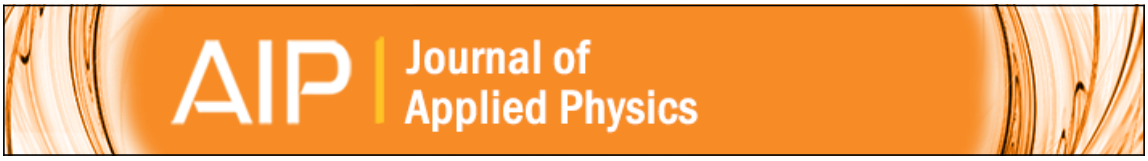

Structure of interfaces in aSi:H/aSiN x :H superlattices

P. V. Santos, M. Hundhausen, L. Ley, and C. Viczian

Citation: Journal of Applied Physics **69**, 778 (1991); doi: 10.1063/1.347364

View online: http://dx.doi.org/10.1063/1.347364

View Table of Contents: http://scitation.aip.org/content/aip/journal/jap/69/2?ver=pdfcov

Published by the AIP Publishing

Structure of interfaces in *a*-Si:H/*a*-SiN$_x$:H superlattices

P. V. Santos[a)]
Institute of Physics Gleb Wataguin, Universidade Estadual de Campinas, P.O. Box 6165, 13081 Campinas-SP, Brazil, and Max-Planck-Institut für Festkörperforschung, Heisenbergstr. 1, D-7000 Stuttgart 80, Germany

M. Hundhausen,[b)] L. Ley,[b)] and C. Viczian
Max-Planck-Institut für Festkörperforschung, Heinsenbergstr. 1, D-7000 Stuttgart 80, Germany

(Received 22 June 1990; accepted for publication 18 September 1990)

We present experimental results on the atomic structure of the interfaces between *a*-Si:H and *a*-SiN$_x$:H layers obtained by analyzing the intensity of the Raman lines from zone-folded acoustic phonons and of the peaks of x-ray diffraction at grazing angles. We determine the width of these interfaces and their stability under thermal annealing in temperatures below the crystallization temperature.

I. INTRODUCTION

The propagation of electromagnetic and of acoustic waves have several aspects in common which arise from the fact that both are wave-like phenomena with linear energy versus wave vector relationship.[1,2] In a superlattice, the periodicity leads to the folding of the dispersion relation of these excitations into mini-Brillouin zones of dimension $2\pi/d$ along the direction perpendicular to the layers (z direction), where d is the superlattice period.[3,4] This holds even in the presence of light absorption or phonon scattering, as long as the inverse absorption coefficient and the phonon coherence length are much larger than the superlattice period. This condition is easily satisfied for small wavelength x rays and for low-frequency acoustic phonons. In addition to the folding, Bragg reflections at the interfaces leads to the opening of energy gaps in the center and at the boundaries of the mini-Brillouin zone. Evidence for the existence of these gaps is found in the observation of additional peaks in the low-angle x-ray diffraction pattern of amorphous superlattices.[5] In the case of acoustic phonons the gaps lead to energy stop bands in the phonon transmission spectra through these structures.[6-8]

The folding of the dispersion relation for acoustic phonons in both crystalline[3,9] and amorphous[10] superlattices has also been verified by the observation of additional lines in the low-frequency Raman spectrum. In these experiments, the incident light suffers Bragg reflections not from the static composition profile of the superlattice but from the dynamic grating created by the modulation of the refractive index of the layers that accompanies the stress induced by the acoustic wave.

The intensity of the x-ray diffraction peaks and of the Raman lines from folded phonons depends on the modulation profile of the superlattice. Recently, several investigations have explored the x-ray diffraction technique to analyze the structure and the composition of amorphous interfaces in superlattices based on hydrogenated amorphous silicon (*a*-Si:H), germanium (*a*-Ge:H), and alloys such as *a*-SiN$_x$:H, *a*-SiC$_x$:H, *a*-SiO$_x$:H and *a*-GeN$_x$:H.[5,11-15] These studies have also been extended to investigate interdiffusion in amorphous materials and the stability of amorphous interfaces under annealing.[13,14,16,20] Previous studies of amorphous interfaces based on Raman scattering have been restricted to the analysis of the high-frequency optical-like phonons.[13,18,19] These vibrations are very sensitive to the local structure of the material and have been used to probe interdiffusion and crystallization of amorphous superlattices.

In this paper, we present a complementary Raman study of interfaces in *a*-Si:H/*a*-SiN$_x$:H superlattices based on the analysis of the intensity of the low-frequency excitation from folded phonons. Specifically, we investigated the width of these interfaces and their stability under thermal annealing at temperatures below the crystallization temperature. The results are confronted with those obtained from x-ray diffraction. The presentation is organized as follows. In Sec. II we present a model for the intensity of the x-ray diffraction peaks. The same model also describes the intensity of the Raman lines from folded phonons. Experimental results obtained in as-grown samples are described in Secs. III A and III B. The effects of temperature annealing on the amorphous interfaces are presented in Sec. III C. In Sec. IV we present a discussion of the experimental data and the main conclusion of this work.

II. SCATTERING INTENSITY IN SUPERLATTICES

In order to extract information about the superlattice interfaces from scattering experiments a relationship is needed between the composition profile of the structure and the scattered intensity. In this section we develop a simple model for the composition profile of the superlattice, from which the intensity of the x-ray reflexes and of the Raman lines from acoustic phonons can be calculated.

In the x-ray experiments that we shall discuss here monochromatic CuK_α ($\lambda = 1.54$ Å) irradiation impinges on the surface of the sample and the intensity of the reflected beam is measured as a function of the incidence angle θ_x.

[a)] Present address: Xerox Palo Alto Research Center, 3333 Coyote Hill Road, Palo Alto, CA 94304.

[b)] Permanent address: Institut für Technische Physik der Universität Erlangen-Nürnberg, Erwin-Rommel-Str. 1 D-8520 Erlangen, Germany.

 0021-8979/91/020778-08$03.00

With respect to the x rays each layer is characterized by a refractive index that depends on the total electron concentration.[21] Several peaks are normally observed corresponding to different Bragg reflection orders.[5] In the absence of resonance effects the intensity of the mth order reflex is proportional to[11,21]

$$I_{x,m} \sim \frac{1}{m^2} K \frac{\tan \theta_{x,m}}{m} \sin \theta_{x,m} |F_{x,m}|^2 \tag{1}$$

where $\theta_{x,m}$ is the incidence angle of the mth reflex. K is a factor which accounts for the polarization of the incident beam and takes the value $(1 + |\cos 2\theta_{x,m}|)/2$ for unpolarized radiation. The factor $F_{x,m}$ is the mth Fourier component of the electronic density profile. This factor is determined by the relative thickness of the layers and by the width and composition profile of the interfaces.

The Raman scattering experiments from acoustic phonons are normally performed in the backscattering geometry with incident light of wavelength λ_L propagating along the superlattice axis. The phonon involved in the process propagates in the same direction and has a wave vector $q = (4n\pi/\lambda_L)$, where n is the effective refractive index of the superlattice at the wavelength λ_L. The scattering leads to a series of doublets of frequencies $\omega_{\pm m} \sim v_{\text{eff}}(q \pm m(2\pi/d))$ in the Raman spectrum, where v_{eff} is the effective longitudinal acoustic (LA) sound velocity along the z direction, and m denotes the folded branch (see Fig. 1 of Ref. 10). This approximation for the phonon frequency is valid for phonon wave vectors q not too close to the center or to the boundary of the mini-Brillouin zone. In this case the Stokes intensity of the Raman peak of frequency ω_m is given by[4]

$$I_{R,m} \sim \omega_m [n_B(\omega_m) + 1] |P_m|^2 \tag{2}$$

where $n_B(\omega_m)$ is the Bose factor. For measurements performed at room temperature, $[n(\omega_m) + 1] \sim kT/\hbar\omega_m$, so that the factor ω_m is cancelled in Eq. (2). The information about the composition profile is contained in P_m, which is the $|m|$th Fourier component of the modulation of the photoelastic coefficient. Within each layer this coefficient specifies how strongly the refractive index of the material is changed by the stress associated with the acoustic phonon.

Equations (1) and (2) establish a relationship between the Fourier components of the spatial modulation of the electronic density and of the photoelastic coefficient, on one side, and the intensity of the x-ray reflexes and of the Raman scattering lines, on the other side. The actual composition profile can, in principle, be obtained by an inverse transformation. This is a simple task for an ideal superlattice, which has a steplike composition profile with perfect parallel layers and abrupt interfaces. A real superlattice, on the other hand, may present a smooth compositional variation at the interfaces due to intermixing of the layer materials. Moreover, layer thickness variations lead to departures from perfect periodicity. Finally, the composition profile may change not only along the growth direction but also perpendicular to it since the interfaces are not perfectly plane and present some roughness. In this case, a more complete model is required to relate all these effects to the Fourier components of the modulation profile.

To take into account material intermixing we will assume a Gaussian error function (erf) profile for the variation in composition across and interface. A superlattice period will then have an effective composition profile given by the following function:

$$f(z) = \frac{1}{2}\left[\text{erf}\left(\frac{z + d_1}{\sigma_m}\right) - \text{erf}\left(\frac{z - d_1}{\sigma_m}\right)\right]$$

for

$$-\frac{d}{2} < z < \frac{d}{2}. \tag{3}$$

Here d_1 and $d_2 = d - d_1$ are the thickness of the superlattice layers and σ_m is the characteristic half-width of the interface due to intermixing effects. Under the assumption that the interface width is much smaller than the individual layer thicknesses ($\sigma_m \ll d_1, d_2$) the square of the mth Fourier transform of $f(z)$, corresponding to a wave vector of magnitude $m(2\pi/d)$, is given by

$$F_m^2 = \left[\frac{4}{m^2\pi^4} \sin^2\left(m\pi \frac{d_1}{d}\right)\right] e^{-(2m\pi \frac{\sigma_m}{d})^2} R_m. \tag{4}$$

The term in square brackets is the structure factor for an ideal two-layer superlattice with abrupt interfaces. Interface broadening due to material intermixing is taken into account by the exponential factor. The latter leads to a strong decrease in the higher-order Fourier components with increasing interface width.

Deviations from perfect periodicity caused by layer thickness fluctuations along the growth direction and by interface roughness are taken into account by the factor R_m in Eq. (4). Such deviations induce incoherent scattering thereby reducing the intensity of the scattering peaks. If these fluctuations are completely random and their amplitude small compared to the nominal layer thicknesses their effect on the Fourier transform of the composition profile is given by a Debye–Waller-like factor of the form[11,21,22]

$$R_m = e^{-(Q_m \sigma_l)^2} e^{-(Q_m \sigma_r)^2} \tag{5}$$

where σ_l and σ_r are the root mean square (rms) amplitude of the layer thickness fluctuations along and perpendicular to the growth direction, respectively. The extended scattering wave vector Q_m is given by $2m\pi/d$ and $(2m\pi/d \pm q)$ for x ray and light scattering, respectively. In the remainder of the paper, we will neglect the contribution q and assume $Q_m = 2m\pi/d$ for the folded phonons.

From the previous equation we conclude that the intensity I_m of the x-ray diffraction peaks and of the Raman lines from folded phonons can be stated as

$$I_m \sim \frac{1}{m^2} \sin^2\left(m\pi \frac{d_1}{d}\right) e^{-\left(2\pi m \frac{\sigma}{d}\right)^2} \tag{6a}$$

where

$$\sigma^2 = \sigma_m^2 + \sigma_l^2 + \sigma_r^2. \tag{6b}$$

Here, σ is an effective interface half-width that takes into account material intermixing, interface roughness, and layer thickness fluctuations. Within the limitations of the present model each one of the effects contribute in the same way to the effective interface thickness $d_i = 2\sigma$. Note that this effec-

tive thickness may in principle be different for x ray and for Raman experiments, since they refer to different physical properties, namely, the modulation profile of the electronic density and of the photoelastic coefficient, respectively.

Finally, we didn't consider in the derivation of Eqs. (5) and (6) the effect of scattering centers within the superlattice layers associated with material inhomogeneities, voids, etc. As we shall see in Sec. III B these centers, when present in a-Si:H/a-SiN$_x$:H multilayers, are probably concentrated near the interfaces. Their effect, in this case, is to increase the interface roughness and they can be taken into account by the term σ_r in Eq. (6).

III. RESULTS

The samples investigated here are a-Si:H/a-SiN$_x$:H superlattices, ($x = 1.3$) grown by the glow discharge decompostion of appropriate gases and having periods ranging from 30 to 400 Å. Their composition modulation was achieved by periodically varying the gas composition in the discharge chamber. The number of a-Si:H/a-SiN$_x$:H double layers in each sample varies with the superlattice period and was chosen to yield a total sample thickness of approximately 1 μ. For comparison, we also included in the following sections results obtained in glow discharge a-Si:H/a-Ge:H superlattices. Further details of the preparation conditions of the a-Si:H/a-SiN$_x$:H and a-Si:H/a-Ge:H superlattices are presented in Ref. 10 and 23, respectively.

A. As-grown samples

The Raman experiments on the a-Si:H/a-SiN$_x$:H amorphous superlattices were performed in the backscattering configuration using an excitation wavelength $\lambda_L = 6471$ Å. A typical Raman spectrum of an as-grown sample (growth temperature $T_a = 280$ °C) is shown in Fig. 1(a). Due to their larger scattering cross section, the scattering is dominated by the a-Si:H layers that have a smaller band gap ($E_{04} = 1.8$ eV) compared to a-SiN$_x$:H ($E_{04} = 4$ eV). For large Raman shifts ($\omega > 100$ cm^{-1})—the high-frequency region—all phonons contribute to the scattering and the spectrum shows broad lines corresponding to maxima in the vibrational density of states of the silicon layers.[24] For low Raman shifts ($\omega < 100$ cm^{-1})—the acoustic region—the spectrum is dominated by narrow lines associated with the excitation of zone-folded longitudinal acoustic phonons [lines ω_1, ω_{-1}, and ω_c in Fig. 1(a)].[10] The peaks labeled ω_1 and ω_{-1} are the normal backscattering lines corresponding to folded phonons with a wave vector $q_z = 2(2n\pi/\lambda_L)$ along the z direction. Line ω_c is due to forward light scattering with $q_z = 0$.[6] This line is observed in the backscattering configuration due to light reflected from the backside of the superlattice film.

In order to obtain information about the composition profile of the superlattice we measured the integrated intensity of the folded phonon lines ω_1 and ω_{-1} for a-Si:H/a-SiN$_x$:H samples with different periods. These integrated intensities depend not only on the modulation profile but also on the optical absorption coefficient and on the total thickness of the samples. To correct for these differences when comparing different samples, the integrated intensities

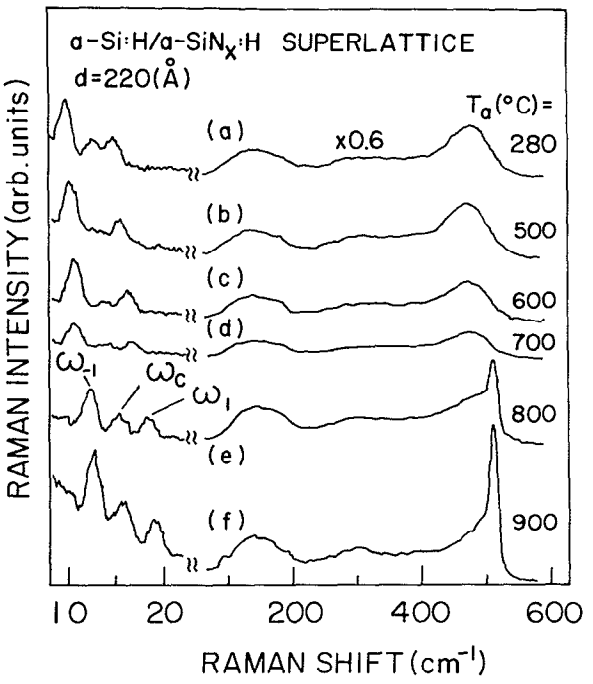

FIG. 1. Raman spectra of a a-Si:H/a-SiN$_x$:H superlattice with a repetition period of 220 Å (a) after growth, and (b)–(f) after annealing at different temperatures T_a. Lines ω_1 and ω_{-1} correspond to the excitation of folded LA phonons with a wave vector $q_z = 2(2n\pi/\lambda_L)$ and line ω_c is due to forward light scattering.

of the first folded phonon doublet was normalized to the total scattering intensity in the high-frequency region [from 100 to 600 cm^{-1}, see Fig. 1(a)]. The normalized intensities calculated in that way will be denoted here by I_R. Following Eq. (6), Fig. 2(a) shows the dependence of the quantity $\ln(I_R/\sin^2(\pi d_2/d))$ vs $(2\pi/d)^2$ for a series of a-Si:H/a-SiN$_x$:H superlattices grown under similar conditions, except for the different thicknesses of the individual a-Si:H (d_2) and a-SiN$_x$:H layers (d_1). From a linear regression of the data we obtain an effective interface thickness $d_i = 18$ Å. For comparison, Fig. 2(b) shows the same plot for a-Si:H/a-Ge:H superlattices. In this case a smaller effective interface thickness of 12 Å is found. We recall here that this effective interface thickness includes both intermixing and layer thickness fluctuations.

Figure 3(a) shows the low-angle x-ray diffraction spectrum of a a-Si:H/a-SiN$_x$:H superlattice with equal thicknesses for the silicon and for the silicon nitride layers. The spectrum was recorded with the Cu$K\alpha$ line corresponding to a wavelength $\lambda_x = 1.54$ Å. Reflexes of order m up to 5 are observed, giving direct evidence for the one-dimensional periodicity of the structure. The small width of the lines (full width at half maximum < 0.1 °C) indicates that there is small fluctuation in the thickness of the individual periods. From the Bragg angle of the reflexes the repetition period was calculated to be 110 ± 1 Å, in good agreement with the nominal value of 104 Å determined from the deposition conditions.

The small intensity of the second order reflex [$I_{x,2}$ in Fig. 3(a)] relative to the reflexes of first ($I_{x,1}$) and of third ($I_{x,3}$) order is consistent with the fact that the silicon and silicon nitride layers have nominally equal thicknesses. Ac-

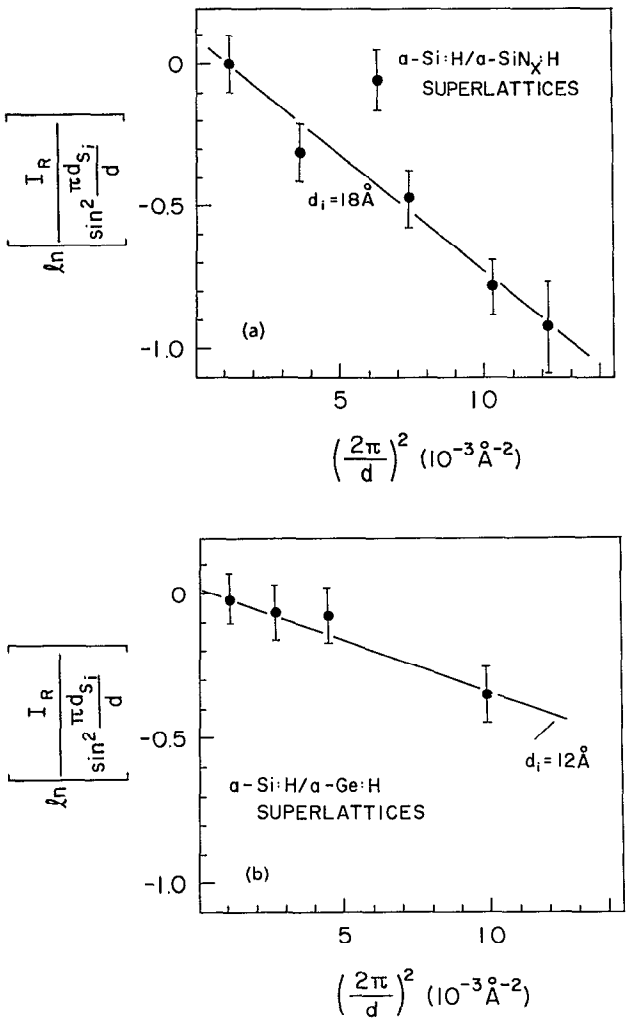

FIG. 2. Normalized intensity of the Raman lines from folded LA phonons as a function of the inverse superlattice period d for (a) a-Si:H/a-SiN$_x$:H and (b) a-Si:H/a-Ge:H superlattices. d_i is the effective interface thickness obtained from a linear regression of the data points.

cording to Eq. (6) the second and higher even order Fourier component of the modulation profile vanish in this case. This result is only valid in the framework of the simple model presented in Sec. II. A complete dynamic theory for the scattering intensity predicts a small but nonvanishing intensity for the second order reflex, even when the two layers have exactly the same thicknesses.[15] The dots in Fig. 3(b) indicate the integrated intensities of the reflexes $I_{x,2}$ and $I_{x,3}$ normalized to the intensity of the first reflex ($I_{x,1}$). The solid lines are the expected intensities for an ideal superlattice ($d_i = 0$ Å), calculated from Eq. (1) for different values of the layer thickness asymmetry $a_s = |(d_1 - d_2)/d|$. All the values are normalized to the intensity $I_{x,1}$ for $a_s = 0$. The relative intensity of the x-ray reflexes, especially of those of higher order, are very sensitive to the relative thicknesses of the layers. The experimental intensities in Fig. 3(b) lie far from the predictions of the model for an ideal superlattice. We note further that these discrepancies cannot be overcome by simply assuming variations in the layer thickness asymmetry from the nominal values. The dashed lines in Fig. 3(b) show the prediction of Eq. (2) by assuming an effective interface thickness equal to the value determined previously from the Raman measurements ($d_i = 18$ Å). As before, all values were normalized to the intensity of the first order reflex for $a_s = 0$. The intensity of the third order reflex is better reproduced in this case. In fact, the agreement to the experimental data is almost perfect if we assume $a_s = 0.1$, as indicated by the crosses in the figure. This indicates that the same effective interface width can be used to explain the intensity of both the Raman and the x-ray lines.

B. Imaging of the interfaces

In order to image the amorphous interfaces a low-energy (1 keV) focused Ar^+ ion beam impinging at grazing incidence was used to etch a small crater on the surface of the superlattice film. The resulting surface morphology was

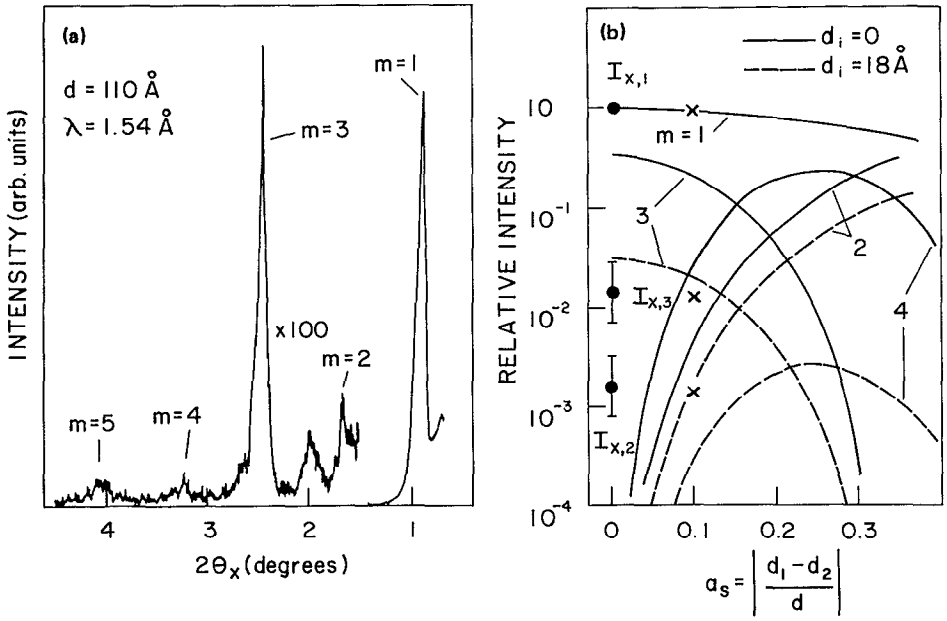

FIG. 3. (a) x-ray diffraction pattern of a a-Si:H/a-SiN$_x$:H superlattice with a repetition period of 110 Å and nominal layer thickness asymmetry $a_s = |(d_1 - d_2)/d|$. The index m specifies the order of the reflexes. The broad structure at $2\theta_x = 2°$ is an artifact of the measurement and is not associated with the superlattice structure. (b) Relative intensity $I_{x,m}$ of the mth reflex as a function of the asymmetry a_s. The symbols are experimental data from the curve in (a) vs the nominal asymmetry (dots) and assuming the asymmetry to be of 0.1 (crosses). The solid (dashed) lines were calculated from Eqs. (1) and (4) for an effective interface width of 0 Å (18Å).

then investigated using an interference contrast microscope. This technique is particularly valuable in revealing inhomogeneities and defects at the interfaces, as we shall see in the following. Figure 4(a) shows an interference micrograph ($\times 40$) of the crater etched into the surface of an a-Si:H/a-SiN$_x$:H superlattice consisting of 23 double layers of silicon and silicon nitride, each 200 Å thick ($d = 400$ Å). The dark contours were identified as the interfaces where a-Si:H is grown on top of an a-SiN$_x$:H layer. The number of contours is equal to the number of periods, i.e., 23 in this particular case.

By surface profiling the edges of the crater with a profilometer we verified that they are smooth and do not present steps at the interfaces. The interference contours can therefore not be assigned to step formation at the superlattice interfaces during ion bombardment. They are attributed to the abrupt lateral variation in the effective optical path of the reflected light at the points where an opaque a-Si:H film begins to cover a transparent a-SiN$_x$:H layer. In the interference microscope, these abrupt phase changes of the reflected light provides the contrast necessary for the observation of the interfaces. At the a-SiN$_x$:H on a-Si:H interfaces, on the other hand, the lateral variations in the optical path are smoother, since the nitride layers are transparent. These interfaces do not present sufficient contrast and cannot be observed in the interference micrographs.

Figure 4(b) shows a section of Fig. 4(a) observed at a higher magnification ($\times 400$). Small bubbles with lateral dimensions of the order of 0.2 μ are seen on the surface of the sample. The bubbles are concentrated along two lines: one along the dark contours, corresponding to the position of the interfaces where a-Si:H is grown on SiN$_x$:H, and the other half-way between the contours, corresponding to the expected position of the SiN$_x$:H on a-Si:H interfaces. The precise origin of the bubbles is unknown. Due to their large dimension compared to the layer thicknesses, they must have been formed during the bombardment. Argon inclusions have been observed in crystalline silicon after bombardment with Ar^+ ions. A similar process could account for the formation of Ar bubbles near the a-Si:H/a-SiN$_x$:H interfaces. Alternatively, the bubbles may be filled with the hydrogen eliminated from the amorphous network as a consequence of the increase in sample temperature during the Ar^+ bombardment. Hydrogen bubbles appear after annealing a-Si:H films.[25] Independently from their origin, a larger concentration of bubbles at the interfaces reveals the presence of an interface transition region where the material is less compact and probably less homogeneous than within the layers.

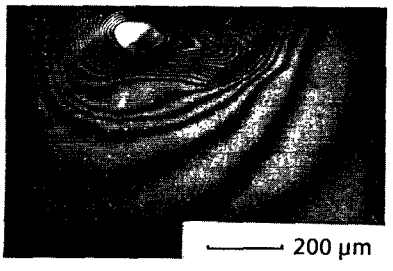

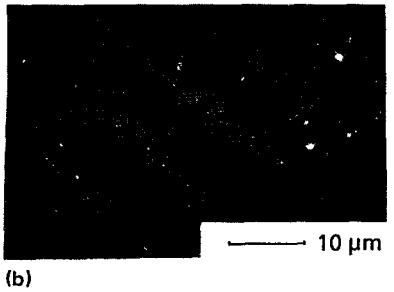

(b)

FIG. 4. Interference micrograph of a crater etched by Ar^+-bombardment into a a-Si:H/a-SiN$_x$:H superlattice with a repetition period of 100 Å observed under an amplification of (a) 40× and (b) 400×. The small bubbles in (b) are concentrated at the position of the interfaces.

C. Annealed samples

In order to investigate the effects of annealing on the structure of the amorphous interfaces the a-Si:H/a-SiN$_x$:H superlattices were annealed in vacuum for 30 min at different temperatures. The structure modifications due to annealing can be appreciated in the series of Raman spectra of Fig. 1. The sample, in this case, is an a-Si:H/a-SiN$_x$:H superlattice with layer thicknesses of 120 and 60 Å for a-Si:H and a-SiN$_x$:H, respectively. In order to increase the interface width artificially, a 20-Å a-SiN$_y$:H layer with a composition $y = 0.6$ was intentionally introduced between each two consecutive layers, so that the sample period is 220 Å.

The spectra in Fig. 1 display two kinds of behavior. For annealing temperatures up to 700 °C [Figs. 1(a) to 1(d)] there is an overall reduction in the scattering intensity with annealing temperature. In this temperature range hydrogen evolves from the a-Si:H layers, reducing its optical gap and increasing the absorption coefficient α for the laser light. The effective sample thickness probed in the Raman experiments ($= 1/2\alpha$) is thereby reduced. The reduction in the scattering volume overcompensates the enhancement in the scattering cross section with increased absorption, leading to a net decrease in the Raman intensity. The increased absorption also leads to the disappearance of the forward scattering line ω_c in the low frequency part of the spectrum, since light reflected at the back surface of the film can no longer reach the front surface.

For annealing temperatures above 700 °C [Figs. 1(e) and 1(f)] there is partial crystallization of the a-Si:H layers, which is signalized by the appearance of a sharp Raman line at 520 cm^{-1}. In agreement with previous observations, we verified that the crystallization temperature increases with decreasing thickness of the silicon layers. The crystallization is accompanied by a reduction in the optical absorption and the forward scattering peak ω_c reappears in the low-frequency range of the spectrum. The folded phonon lines are observed for annealing temperatures far above the crystallization onset. This is direct evidence that the superlattice structure is not destroyed during the annealing process.

The folded-phonon lines in Fig. 1 shift to higher frequencies with increasing annealing temperature. The frequency increase is gradual up to 700 °C. The crystallization onset between 700 and 800 °C is followed by an abrupt frequency shift. The frequency of the folded-phonon lines is proportional to the inverse period $1/d$ and to the average

sound velocity for LA waves in the superlattice. An analysis of the x-ray diffraction pattern of annealed samples reveals that the repetition period reduces at most 5% when the sample is annealed to 750 °C. The large frequency shifts in Fig. 1 (20%–30%) are then predominantly due to an annealing induced increase in the effective sound velocity. Below the crystallization temperature, this effect can be associated with hydrogen evolution. In fact, sound velocity measurements in unstructured *a*-Si:H layers show a strong dependence on hydrogen concentration.[26] The abrupt frequency shifts at the crystallization onset is explained by the higher sound velocity of the crystalline material.

In order to analyze the effects of annealing on the modulation profile of the superlattices we plot in Fig. 5 the integrated intensity of the lines ω_{-1} and ω_{+1}, normalized to the total scattering intensity in the optical region, as a function of the annealing temperature. Strictly speaking, the normalization procedure only applies for annealing temperatures below the crystallization onset (indicated by arrows in Fig. 5), where there is no substantial change in the high-frequency part of the Raman spectrum. According to Eqs. (2) and (4) the normalized intensities are proportional to the first harmonic of the effective composition profile. The data are presented for two samples with periods of 110 and 220 Å, respectively. In both cases a clear maximum is found for annealing temperatures around 650 °C. Instead of smearing out due to interdiffusion, the effective composition profile of the interfaces seems to become steeper after annealing around 650 °C. Note that the effect takes place far below the crystallization temperature (see arrows in Fig. 5), i.e., in a range where there is practically no change in the high-frequency part of the Raman spectrum.

A similar effect has also been observed in the low-angle x-ray diffraction pattern of the samples. Figure 6 shows a series of x-ray spectra of a *a*-Si:H/*a*-SiN_x:H sample with a period of 110 Å recorded after annealing at different temperatures. In agreement with previous investigations,[13] the diffraction peaks can be observed in samples annealed at least up to 750 °C, indicating again the high stability of the interfaces against interdiffusion. As in the case of folded phonons, the intensity of the reflexes increases strongly when the sample is annealed at 650 °C and decreases for higher temperatures.

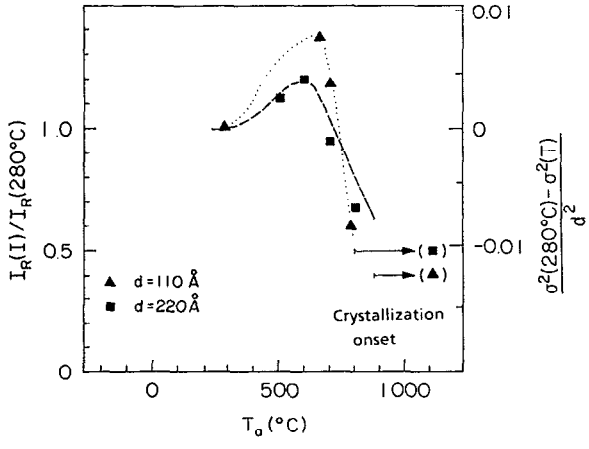

FIG. 5. Normalized intensity of the Raman lines from folded LA phonons as a function of the annealing temperature for two *a*-Si:H/*a*-SiN_x:H superlattices with periods of 110 and 220 Å. The normalization was performed by dividing the integrated intensity of the Raman lines from folded phonons by the integrated scattering intensity in the range from 100 to 600 cm^{-1}.

The changes in the intensity of the x-ray reflexes can be due to a reduction either in the effective interface width or in the relative thickness of the superlattice layers [see Fig. 3(b)]. The latter mechanism plays a secondary role in the case of our samples. To see this we recall that the 110 Å sample of Fig. 6 has *a*-Si:H and *a*-SiN_x:H layers with nominally the same thickness. This accounts for the small intensity of the $m = 2$ line relative to the others. According to Eqs. (2) and (4) the intensity of the first Raman doublet ($m = \pm 1$) is maximal in this case: any appreciable deviation from the condition $d_1 = d_2$ induced by the annealing would cause the scattering intensity in Fig. 5 to reduce. That is not the case, at least for annealing temperatures below 650 °C.

We attribute the line intensity behavior to a reduction in the effective interface width when the *a*-Si:H/*a*-SiN_x:H superlattices are annealed around 650 °C. In order to estimate the interface width as a function of the annealing temperature we shall assume that changes in the layer thickness asymmetry during annealing can be completely disregarded. In this case the relative variation in the interface width $\delta_d^2(T)$ defined by:

$$\delta_d^2(T) = \frac{\sigma^2(280\,°C) - \sigma^2(T)}{d^2} = \frac{d_i^2(280\,°C) - d_i^2(T)}{4d^2} \tag{7}$$

is proportional to the intensity ratio $I_R(T)/I_R(280\,°C)$. This quantity is plotted on the right-hand side of Fig. 5. The 110-Å period sample has an initial interface width of $d_i(280\,°C) = 18 \pm 2$ Å. Taking $\delta_d(650\,°C) = 0.008$ we calculate the effective interface thickness at 650 °C to have decreases to less than ~8 Å. For the sample with a period of 220 Å. A similar analysis cannot be performed since a 20 Å layer of *a*-$SiN_{0.6}$:H was artifically introduced at each interface. Nevertheless if we assume the initial interface thickness to lie in the range from 30 to 40 Å (the 20-Å thick *a*-$SiN_{0.6}$:H layer plus two adjacent interfaces, each ~9 Å thick) we obtain an effective interface thickness at 650 °C smaller than ~20 Å.

IV. DISCUSSIONS AND CONCLUSIONS

The analysis of the intensity of the x-ray peaks and of the Raman lines from folded phonons presented above yield effective interface widths of 18 and of 12 Å for as-grown *a*-Si:H/*a*-SiN_x:H and *a*-Si:H/*a*-Ge:H superlattices, respectively. In the case of *a*-Si:H/*a*-Ge:H superlattices, investigations of the interface thickness based on Raman scattering from high-frequency phonons[18,19] have concluded that the composition changes take place in a region not exceeding one or two atomic monolayers. *a*-Si:H/*a*-Ge:H superlattices constitute a well-behaved case where the two materials have similar short-range order and where the mismatch in the atomic distances can be easily accommodated in a mono-

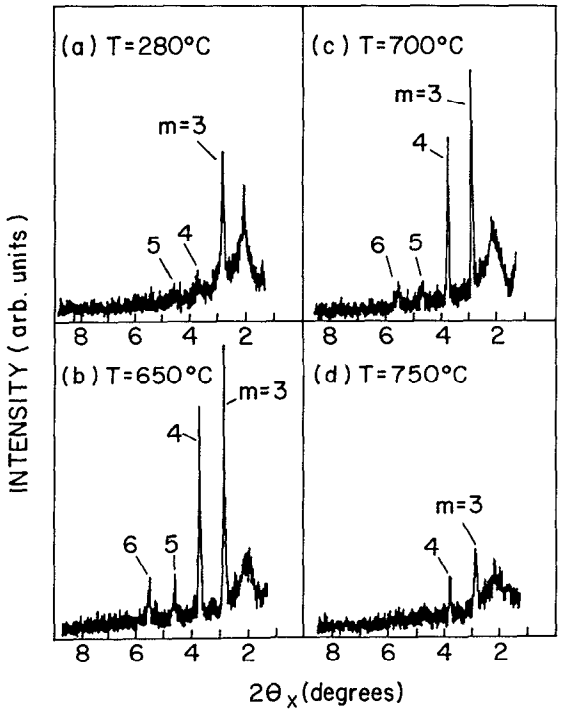

FIG. 6. x-ray diffraction pattern of a a-Si:H/a-SiN_x:H superlattice with repetition period of 100 Å (a) after growth and (b)–(d) after annealing at different temperatures. As in Fig. 2(a), the broad structure at $2\theta_x = 2°$ is an artifact of the measurement and is not associated with the superlattice structure.

layer-thick amorphous interface. The apparent contradiction with our results is resolved if we take into account that the latter experiments probe only the local composition of the interfaces. They are thus not sensitive to interface roughness or to layer thickness fluctuations during the growth. Assuming the width of the interfaces due to intermixing to be 6 ± 1 Å,[18,19] we calculate the rms amplitude of the interface roughness to be of $\sigma_s \sim \sqrt{12^2 - 6^2}/2 \sim 5$ Å. In this analysis we neglected contributions from layer thickness fluctuation during sample growth, which are expected to be very small in the computer-controlled deposition system used to grow the samples.

The situation is different for a-Si:H/a-SiN_x:H superlattices, where the short-range order is considerably different in the two materials. Although there can be abrupt changes in the concentration profile of silicon and nitrogen at each interface, this change is likely to be accompanied by considerable distortions of the network near the interfaces in order to accommodate the structural differences. Although there can also be an abrupt change in the local composition profile for silicon and nitrogen at each interface, the materials within the layers are considerably distorted in the proximity of the interface in order to accommodate the structural differences.[27,29] Infrared absorption studies in glow discharge a-Si:H/a-SiN_x:H superlattices revealed that the interfaces are rich in hydrogen.[28,29] The presence of bubbles at the a-Si:H/a-SiN_x:H interfaces in Ar^+-etched samples is probably associated with the presence of a low-density interface layer with higher hydrogen content. Therefore we expect the density profile and the profile for the photoelastic coefficient across the interface to be less abrupt than in a-Si:H/a-Ge:H samples. Interface roughnesses further contribute to an increase in the effective interface thickness. As we mentioned previously, it is not possible to separate the two effects based solely on the simple model presented in Sec. II.

The two kinds of superlattices exhibit opposite behavior under annealing. In a-Si:H/a-Ge:H, annealing at relative low temperatures ($\sim$400 °C) leads to strong material intermixing followed by the crystallization of the resulting silicon germanium alloy.[20] a-Si:H/a-SiN_x:H samples, on the other hand, are stable even for annealing temperatures high enough to induce the crystallization of the a-Si:H layers. There is no evidence for material intermixing in this case. In fact, the effective interface width of the a-Si:H/a-SiN_x:H interfaces actually reduces for annealing temperatures around 650 °C. The x-ray diffraction experiments also reveal a decrease in the superlattice period with annealing. We attribute this behavior to the compaction of the material near the interfaces that follows hydrogen evolution. As a consequence, the silicon and silicon nitride layers become more homogeneous, leading to a reduction in the effective interface thickness.

In the following we discuss possible reasons for the interface narrowing induced by thermal annealing around 650 °C. The interfaces between the a-Si:H and the SiN_x:H layers in a freshly deposited a-Si:H/a-SiN_x:H superlattice may have a finite width over which the composition varies continuously from pure a-Si:H to pure a-SiN_x:H as a result of material mixing during sample growth. The interface compaction takes place without further intermixing, and there can even be a reduction in the intermixing range between the two layers. In fact, when a nonstoichiometric SiN_y:H alloy, $x \neq 1.33$, is annealed, a-Si:H-rich and a-$SiN_{1.33}$-rich clusters are initially formed through material diffusion.[30] The crystallization takes place only after this initial phase separation. This occurs because the sole crystalline phase containing only silicon and nitrogen is silicon nitride (Si_3N_4), so that nonstoichiometric silicon nitride must separate into this phase and pure silicon, before it can crystallize. The material diffusion in the composition gradient presented at the interfaces is determined by two opposite driving forces. The first one is associated with the gain in chemical energy through the formation of the stoichiometric compounds. This force favors the phase separation at the interfaces and yields a negative contribution to the effective diffusion coefficient. The second driving force is related to the entropy gain when there is a mixing of the materials, leading to a positive contribution of the diffusion coefficient.[17] The first mechanism dominates in a-Si:H/a-SiN_x:H superlattices, leading to an effective diffusion coefficient that is negative. The silicon and nitrogen atoms at the interface diffuse, therefore, in the direction of the silicon and of the silicon nitride layers, respectively, leading to a narrowing of the interfaces for annealing temperatures up to 650 °C. Similar behavior has been reported for metallic Cu/Ni superlattices.[31] Silicon-germanium alloys, on the other hand, can crystallize for all compositional ranges and strong material intermixing takes place before crystallization.

For higher annealing temperatures, the effective interface width decreases, as is evident in Figs. 5 and 6. In this temperature range the *a*-Si:H layers crystallize partially. The interface broadening in this case is probably associated with an increase in interface roughness when crystallization occurs.

In summary, we showed that x-ray and Raman scattering measurements can be successfully used to probe the structure and the stability of interfaces in amorphous superlattice structures. As-grown *a*-Si:H/*a*-SiN_x:H and *a*-Si:H/*a*-Ge:H interfaces have effective thicknesses of 18 and 12 Å, respectively. The interface thickness includes material intermixing effects, layer thickness fluctuations during growth, and interface roughness. In contrast to *a*-Si:H/*a*-Ge:H, the *a*-Si:H/*a*-SiN_x:H are very stable under annealing, even for temperatures above the crystallization temperature of the *a*-Si:H layers. We further verified that the interface thickness decreases for annealing around 650 °C. This behavior was attributed to interface compaction followed by a phase separation of the interface material.

ACKNOWLEDGMENTS

We thank Professor I. Chambouleyron for discussions and for a critical reading of the manuscript, and Dr. M. Hoffmann from the Max-Planck-Institut fuï Metallforschung, Stuttgart, Germany, for the Ar^+ ion etch of the multilayers. One of us (P.V.S.) acknowledges the financial support from CNPq and from FAPESP, Brazil.

[1] L. M. Brekhovskikh, *Waves in Layered Structures* (Academic, New York, 1960).
[2] P. V. Santos, PhD. dissertation, University of Stuttgart, 1988.
[3] C. Colvard, R. Merlin, M. V. Klein, and A. C. Gossard, Phys. Rev. Lett. **45**, 298 (1980).
[4] C. Colvard, T. A. Grant, M. V. Klein, R. Merlin, R. Fisher, H. Morkoç, and A. C. Gossard, Phys. Rev. B **31**, 2080 (1985).
[5] B. Abeles and T. Tiedje, Phys. Rev. Lett. **51**, 2003 (1983).
[6] P. V. Santos, L. Ley, J. Mebert, and O. Koblinger, Phys. Rev. B **36**, 4858 (1987).
[7] O. Koblinger, J. Mebert, E. Dittrich, S. Döttinger, W. Eisenmenger, P. V. Santos, and L. Ley, Phys. Rev. B **35**, 9372 (1987).
[8] V. Naranayamurti, H. L. Stormer, M. A. Chen, A. C. Gossard, and W. Wiegmann, Phys. Rev. Lett. **43**, 2012 (1979).
[9] B. Jusserand and M. Cardona, in *Light Scattering in Solids V*, edited by M. Cardona and G. Güntherodt (Springer, Berlin, 1989), p. 49.
[10] P. V. Santos, M. Hundhausen, and L. Ley, Phys. Rev. B **33**, 1516 (1986).
[11] B. Abeles, T. Tiedje, K. S. Liang, H. W. Deckman, H. C. Stasiewski, J. C. Scanlar, and P. M. Eisenberger, J. Non-Cryst. Solids **66**, 351 (1984).
[12] S. Miyazaki, Y. Kohda, Y. Hazama, and M. Hirose, in *Proceedings of the 13th International Conference on Amorphous and Liquid Semiconductors*, edited by M. A. Paesler, S. C. Agrawal, and R. Zallen (North-Holland, Amsterdam, 1989), p. 774.
[13] J. Gonzalez-Hernandez, D. D. Allred, and O. V. Nguyen, in *Material Research Society Symposium Vol. 77*, edited by J. Dow and I. Schuller (Material Research Society, New York, 1987), p. 665.
[14] K. Tanaka, I. Honma, H. Tamaoki, and H. Komiyama, in *Materials Research Society Symposium Vol. 118*, edited by A. Madan, M. J. Thompson, P. C. Taylor, Y. Hamakawa, and P. G. LeComber (Material Research Society, Pittsburgh, 1988), p. 343.
[15] P. D. Persans, A. F. Rupert, B. Abeles, G. Hughes, and K. S. Liang, in *Material Research Society Symposium Vol. 149*, edited by A. Madan, M. J. Thompson, P. C. Taylor, Y. Hamakawa, and P. G. LeComber (Material Research Society, Pittsburgh, 1989), p. 711.
[16] S. M. Prokes and S. Spaepen, Appl. Phys. Lett. **47**, 234 (1986).
[17] F. Spaepen, in *Material Research Society Symposium Proceedings (Symposium on Epitaxy and Layered Structures)*, edited by J. M. Gibson and L. R. Dawson (Material Research Society, New York, 1985), p. 295.
[18] P. V. Santos and L. Ley, Phys. Rev. B **36**, 3325 (1987).
[19] P. D. Persans, A. F. Rupert, B. Abeles, and T. Tiedje, Phys. Rev. B **32**, 5558 (1985).
[20] P. D. Persans, A. Rupert, and B. Abeles, J. Non-Cryst. Solids **102**, 130 (1988).
[21] J. H. Underwood and T. W. Barbee, in *Low Energy X-Ray Diagnostics, AIP-Conference Proceedings No. 75*, edited by D. T. Atwood and B. L. Henke (American Institute of Physics, New York, 1981), p. 170.
[22] N. W. Ashcroft and N. D. Mermin, *Solid State Physics* (Holt, Rinehart and Winston, Philadelphia, 1981), p. 790.
[23] P. V. Santos and L. Ley, Phys. Rev. B **36**, 3325 (1987).
[24] J. E. Smith, Jr., M. H. Brodsky, B. L. Crowder, M. I. Nathan, and A. Pinczuk, Phys. Rev. Lett. **26**, 642 (1971).
[25] H. R. Shanks and L. Ley, J. Appl. Phys. **52**, 811 (1981).
[26] M. Grimsditch, W. Senn, G. Winterling, and M. H. Brodsky, Solid State Commun. **26**, 229 (1978).
[27] C. B. Roxlo, B. Abeles, and T. Tiedje, Phys. Rev. Lett. **52**, 1994 (1984).
[28] C. B. Roxlo, B. Abeles, and P. D. Persan, J. Vac. Sci. Technol. B **4**, 1430 (1986).
[29] B. Abeles, L. Yang, P. D. Persans, H. S. Stasiewski, and W. Lanford, Appl. Phys. Lett. **48**, 168 (1986).
[30] A. Morimoto, T. Takaoka, M. Kumeda, and T. Shimizu, Philos. Mag. B **50**, 517 (1984).
[31] T. Tsakalatos, Acta Metall. **15**, 255 (1982).